communications earth & environment

Article

https://doi.org/10.1038/s43247-024-01934-2

Historical changes in the Causal Effect Networks of compound hot and dry extremes in central Europe

Check for updates

Yinglin Tian [1,2,11] ✉, Domenico Giaquinto [3,4,11], Giorgia Di Capua[1,5], Judith N. Claassen[6], Javed Ali [7,8], Hao Li [9] & Carlo De Michele [10]

Changes in hot and dry extremes in central Europe have been attributed to atmospheric circulation anomalies and land-atmosphere interactions. However, the strength of the underlying causal links and their historical trends have not been quantified. Here, we use Causal Effect Networks (based on the Peter and Clark momentary conditional independence algorithm) and show that hot extreme events in central Europe are driven primarily by anomalous atmospheric patterns and soil water deficiency. Dry extreme events are mainly induced by anomalous atmospheric patterns and soil moisture memory, and only marginally by temperature changes. We find that in the period 1979–2020, the influence of dry soil on temperature has been amplified by 67% during compound hot and dry extremes, while the impact of atmospheric drivers on soil moisture has intensified by 50% (36%) during compound (single) extremes. This work highlights the strengthened causal links of compound hot and dry extremes with their underlying drivers under global warming, which can lead to non-linear interactions and increase adaptation challenges.

Anthropogenic global warming continues to set new records. 2023 was the warmest calendar year on record: for the first time, the mean global surface temperature has exceeded every day 1 °C above the pre-industrial level[1]. Accordingly, 2023 boreal summer (June, July, and August) was the warmest season, with August and July 2023 being the warmest months in the ERA5 data record[1]. In Europe, while the 2022 summer was the hottest ever recorded, summer 2023 was the fifth warmest, with temperatures 0.83 °C higher than average[2].

Heatwaves pose a serious threat to human health, as shown by the increase of high temperature-related fatalities in Europe[3]. According to the World Meteorological Organization, heatwaves are the most impactful weather hazard in Europe by far, being responsible for up to 93% of deaths resulting from weather-, climate-, and water-related extremes in the 1970–2019 period[4]. Furthermore, the occurrence of European heatwaves has increased almost four times faster compared to the rest of the northern midlatitudes over the past 42 years, making Europe one of the main heatwave hotspots worldwide[5]. According to Zschenderlein et al.[6], the most prominent physical mechanisms that lead to the occurrence of heatwave are adiabatic heating following subsidence, advection of warm air at the surface level, and diabatic heating due to surface sensible heat fluxes or incoming solar radiations[7]. The combination of adiabatic warming and high radiative heating due to clear-sky conditions could lead to persistent and intense anomalous Rossby waves, thus enhancing the increase of surface temperatures[8].

If on the one hand, it is straightforward to understand that a warmer atmosphere leads to higher surface temperatures, its impact on wet-dry conditions is more complex. According to thermodynamics principles, air moisture holding capacity increases with warmer temperatures[9,10], thus assuming constant relative humidity and neglecting dynamical aspects, more rainfall extremes due to global warming are expected. Nevertheless, high temperatures often sustain dry conditions as well, leading to water scarcity and soil moisture depletion, following a positive soil moisture-

[1]Earth System Analysis, Potsdam Institute for Climate Impact Research (PIK)—Member of the Leibniz Association, Potsdam, Germany. [2]State Key Laboratory of Hydroscience and Engineering, Department of Hydraulic Engineering, Tsinghua University, Beijing, China. [3]Complexity Science, Potsdam Institute for Climate Impact Research (PIK)—Member of the Leibniz Association, Potsdam, Germany. [4]Modeling and Engineering Risk and Complexity, Scuola Superiore Meridionale, Naples, Italy. [5]Department of Water, Environment, Construction and Safety, Magdeburg-Stendal University for Applied Sciences, Magdeburg, Germany. [6]Institute for Environmental Studies (IVM), Vrije Universiteit Amsterdam, Amsterdam, the Netherlands. [7]Department of Civil, Environmental and Construction Engineering, University of Central Florida, Orlando, FL, USA. [8]National Center for Integrated Coastal Research, University of Central Florida, Orlando, FL, USA. [9]Hydro-Climate Extremes Lab, Ghent University, Ghent, Belgium. [10]Department of Civil and Environmental Engineering, Politecnico di Milano, Milan, Italy. [11]These authors contributed equally: Yinglin Tian, Domenico Giaquinto. ✉e-mail: yinglin.tian@pik-potsdam.de

temperature feedback process[11,12]. The dual increase of these extreme conditions was manifested in Europe during 2023, where high temperatures led to dry soils and drought conditions in the southern part of the continent, with the spreading of numerous wildfires across the Mediterranean region[13].

Therefore, given the numerous mechanisms behind drought developments, it is crucial to distinguish among different types of water scarcity, whether they are related to a lack of precipitation, soil humidity, water or groundwater discharge, and freshwater availability for society. The aforementioned drought definitions are associated with different variables and could be driven by different atmospheric processes[14,15]. A direct impact of climate change on precipitation decline has been detected for the Mediterranean region[16], while dry conditions over central and northern Europe are likely more related to the increased evaporative losses and reduced soil moisture caused by warmer temperatures[11,17].

The impacts and cascading effects of drought events also depend on the timescales at which these events develop. Generally, droughts are slowly evolving phenomena, which are usually evaluated on a monthly basis[18]. However, low levels of precipitation combined with extreme temperatures can result in fast transitions to dry conditions on sub-monthly scales, leading to flash droughts[19]. These dry extremes recently gained attention due to their devastating and sudden impacts on crop yields and water supply all around the globe[20–22], as soil water content is strongly affected due to the abrupt increase of evaporative demand[23]. To capture the short duration of flash droughts, previous studies have analyzed these events setting the temporal resolution to the pentad scale, i.e., a series of 5 consecutive days[24,25], also in line with the typical duration of hot extremes, which develop on timescales of at least 3 days[26,27]. Therefore, the pentad timescale is also adopted in this study to capture both hot and dry conditions.

When heatwaves and droughts co-occur, their impacts can be exacerbated, leading to more serious negative effects both on the ecosystem and society. For instance, co-occurring heatwaves and droughts can lead to a higher likelihood of crop failures, tree mortality, wildfires, reduced streamflow, and greater water shortage[28]. Such co-occurring extremes have been classified as compound events, i.e., situations where two or more hazards/drivers co-occur and are responsible for enhanced weather and climate-related impacts[3,29,30].

Throughout the last decade, an increase in hot and dry events has been observed globally[29,31], and this increasing trend is expected to continue with global warming[32]. Therefore, it is urgent to quantify the joint occurrence of these hazards, as highlighted in the IPCC 6th assessment report[33,34], and to investigate the interdependencies between different drivers of hot and dry compound events, aiming at reducing their impacts with more accurate predictions and early warning systems[31].

Compound hot and dry events can be triggered by both local and large-scale drivers on a variety of temporal scales. Mukherjee et al.[31] identify local conditions such as vapor pressure deficit, potential evaporation, and precipitation as important variables. Next to thermodynamic ones, dynamic drivers such as large-scale atmospheric circulation patterns have been identified[29] as precursors of hot and dry events as well: the prevalence of long-lasting high-pressure systems often leads to prolonged hot conditions and reduced precipitation[35]. However, the complex interactions between local thermodynamic effects and large-scale remote atmospheric drivers may also influence the intensity and duration of compound hot and dry extremes[36]. Hence, understanding the causal relationships between both local and larger-scale climate drivers for a specific region can provide a holistic understanding of these events.

Recent studies have investigated the drivers of compound hot and dry events by using probabilistic methods to assess the dependence between the two[28,37]. A clear distinction between the mechanisms behind single and compound extremes could be beneficial to improve sub-seasonal to seasonal forecasts and to implement appropriate adaptation measures. Moreover, the detection and quantification of causal pathways of compound events remains an open question.

Causal analysis has been gaining attention in the field of climate science as it has shown to be useful to deepen our understanding of the physical relationships among various processes and variables of the Earth system. Indeed, causal algorithms are capable of detecting directional dependencies ruling out spurious correlations resulting from random coincidence[38]. Several causal methods have been applied to Earth System Science[39]. For instance, traditional Granger causality[40,41] is based on linear auto-regressive models to address bivariate causal associations. If on the one hand this interpretation of the model is straightforward, on the other hand, it is limited to linear and stationary bivariate time series[39]. Moreover, if the system under study is made by weakly coupled subsystems, Granger causality may fail[42]. In this case, more refined methodologies, like convergent cross mapping (CCM)[43,43,44] may help, enabling the detection of causality in deterministic nonlinear dynamic systems with weak to moderate couplings and non-separable variables[45].

Here, we employ Causal Effect Networks (CENs) obtained with the Peter and Clark momentary conditional independence (PCMCI) algorithm[46], a method based on the conditional independence framework which allows to investigate causal associations in large time series datasets. In the context of our analysis, PCMCI offers several strengths with respect to other methodologies like CCM. First of all, it is suited to handle conditioning on multiple variables without excessive computational cost, making it a practical choice for complex, large-scale data. Moreover, it can be applied both in a linear and nonlinear manner, making it more flexible to different research scenarios. In the present study, we employ it under a linear framework, in conjunction with conditional partial correlation. This is done to allow a clear interpretation of the found relationships, bridging the gap between statistical analysis and physical mechanisms. PCMCI has successfully been applied to detect causal relationships in the Earth system, such as the boreal summer tropical—extratropical links[47], the Atlantic hurricane activity[48], polar vortex dynamics[49], the North Atlantic Oscillation (NAO), and Mediterranean winter temperatures[50] and the Indian summer monsoon[51].

Hence, in this study we aim to (i) quantify the causal links from potential remote and local drivers to single and compound hot and dry extremes in central Europe, (ii) assess the prediction power of the identified causal drivers, and (iii) investigate the evolution of the causal links with time and varying temperature/soil humidity conditions. In particular, we focus on the causal relationships between Water Surplus/Deficit (WSD), 2 m air temperature (T2m), and atmospheric precursors (i.e., Z500—geopotential height at 500 hPa height). We find that global warming can exacerbate hot and dry extreme conditions by linearly increasing the strength of the causal drivers, as well as impact the strength of causal links in a nonlinear manner.

Results

Atmospheric circulation patterns of hot and dry extremes

Throughout this study, we use daily data from the ERA5 reanalysis dataset[52] with a spatial resolution of 1° × 1°, averaged on 5-day time steps, considering the typical durations of the synoptic high-pressure systems and hot/dry events. In Fig. 1a, b, we show T2m and WSD anomalies in August 2003 over central Europe (CEU), where we observe a T2m positive anomaly of 3.2 K and a WSD negative anomaly of −2.3 mm per day. During the 1979–2020 period, the frequency of hot extremes ($T2m > T2m_{95th}$) has significantly increased in CEU at the rate of 0.5 events per decade, while their magnitude, i.e., the seasonal-mean T2m anomaly of hot extremes, shows a non-significant slight increase (0.002 K per decade, Fig. 1c, d). As for dry extremes ($WSD < WSD_{5th}$, Fig. 1e, f), the magnitude, i.e., the absolute seasonal-mean WSD anomaly of dry extremes, has significantly intensified at the rate of |−0.2| mm per day per decade, while the frequency also increased (0.17 events per decade), non-significantly.

Anomalous atmospheric circulation has been suggested as a potential driver of hot or dry extremes. Figure 2 shows composites of 500-hPa geopotential height (Z500) anomalies in the Northern Hemisphere from two pentads before to after single hot (Fig. 2a), single dry (Fig. 2b), and compound extremes ($T2m > T2m_{95th}$ and $WSD < WSD_{5th}$, Fig. 2c) in the CEU region. When comparing the composites shown in Fig. 2a–c, a consistent pattern emerges, i.e., a high-pressure system over central Europe together

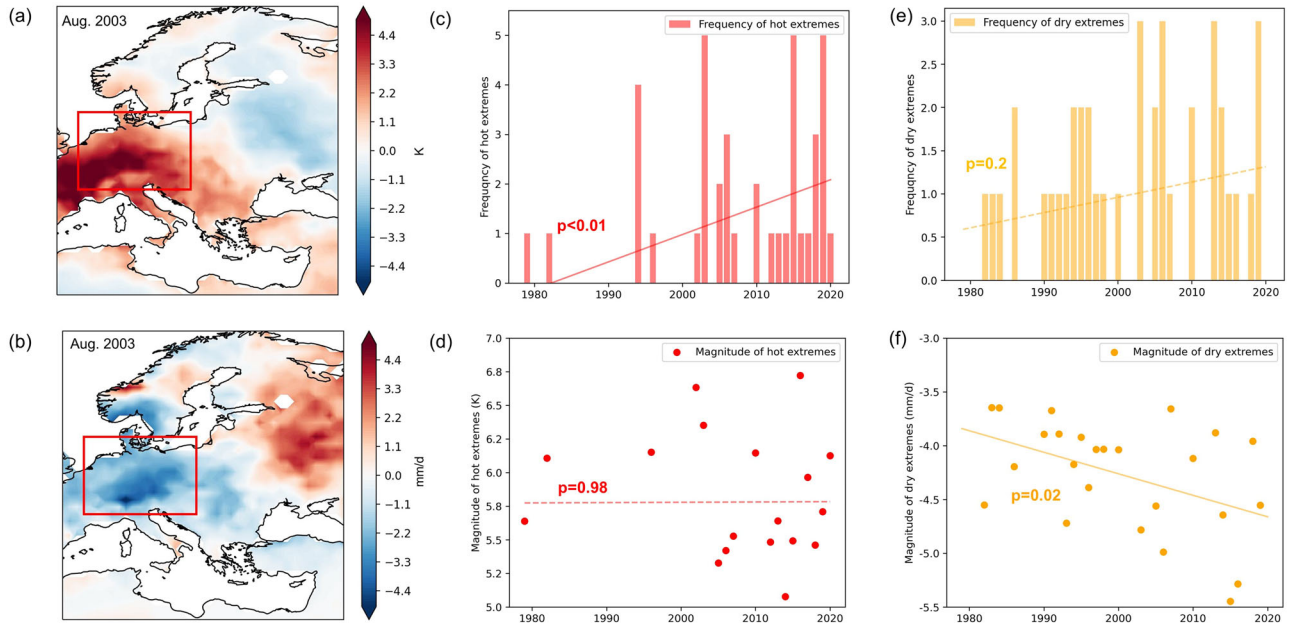

Fig. 1 | Study region and trends of hot and dry extremes in central Europe. a T2m and **b** WSD anomalies in August 2003 over CEU, marked by the red rectangle. **c–f** Interannual variations in frequency (**c, e**) and magnitude (**d, f**) of hot (T2m > $T2m_{95th}$) (**c, d**) and dry (WSD < WSD_{5th}) (**e, f**) extremes in CEU. In (**c–f**), magnitude is the seasonal-mean T2m (WSD) anomaly of the hot (dry) extremes; solid lines represent a significant linear regression with $p < 0.05$, while dashed lines are non-significant linear regression.

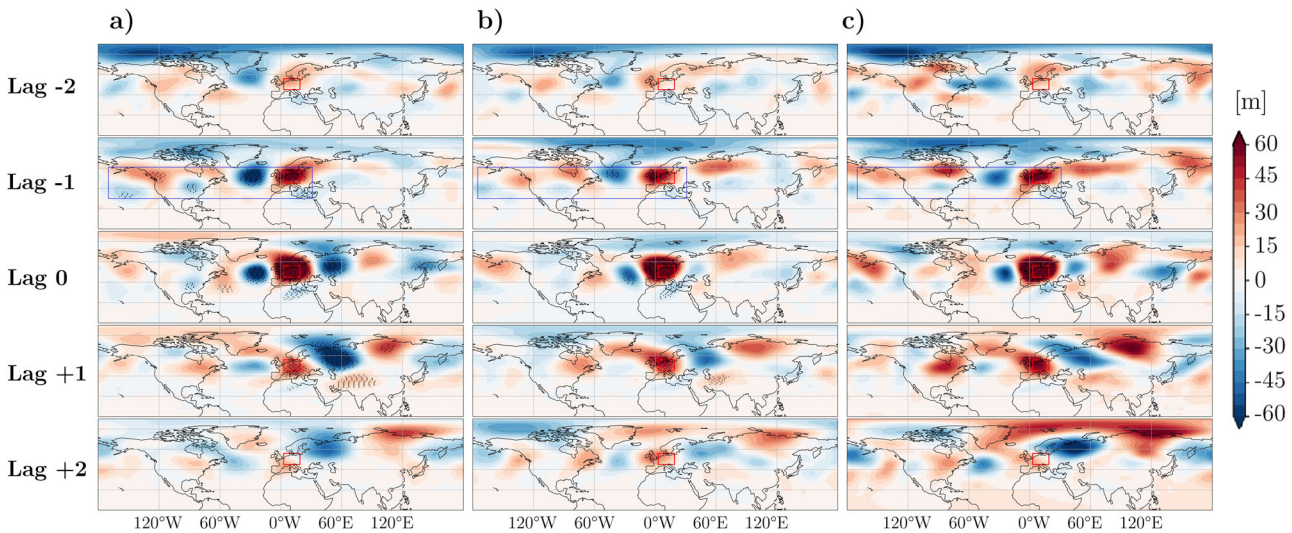

Fig. 2 | Anomalous atmospheric circulation before and after single and compound hot and dry extremes in central Europe. Composites of Z500 fields for **a** single hot extremes (T2m > $T2m_{95th}$), **b** single dry extremes (WSD < WSD_{5th}), and **c** compound hot and dry extremes (T2m > $T2m_{95th}$ and WSD < WSD_{5th}) in central Europe (CEU). The composites are computed from two pentads before to two pentads after the extremes (from the top row to the bottom row). The red box represents the CEU region, while the blue box is the precursor region used to evaluate the atmospheric conditions influencing CEU. Black dots are drawn if the Z500 anomaly is significant at $\alpha = 0.05$.

with a low-pressure system in the North Atlantic. However, while during hot extremes the wave shows to propagate eastward, covering the eastern North Pacific, North America, the North Atlantic, central Europe, and central Siberia (lag −1 to lag 1, Fig. 2a), during dry extremes the high-pressure system over central Europe persists up to lag 1 (Fig. 2b). During compound extremes, both the wave propagation and the persistent high pressure over CEU are observed (Fig. 2c). To analyze the atmospheric precursors of single and compound hot and dry extremes, we construct three-time series, namely the $Z500_T$, $Z500_W$, and $Z500_c$ indices. These are one-dimensional time series which represent the linear correlation at each pentad time step between the respective composite field at lag −1 (i.e., 5 days prior to the extremes) and the Z500 field over the blue rectangle (30°*N*–60°*N*, 170°*W*–30°*E*) shown in Fig. 2. The choice of the representative area of the atmospheric precursors is based on their hindcast ability on T2m and WSD (see Supplementary material for further details, Figs. S1, S2, and Supplementary note S1). The atmospheric precursors are evaluated only at lag −1 because in this case the composite signals are both intense and significant, especially over CEU, which is not true in the case of lag −2 (see Fig. 2).

Next, we investigate the correlation (via the Pearson coefficient and conditional probability) between the atmospheric precursors identified in Fig. 2 and the occurrence of hot and dry extremes (Fig. 3). Summer T2m and

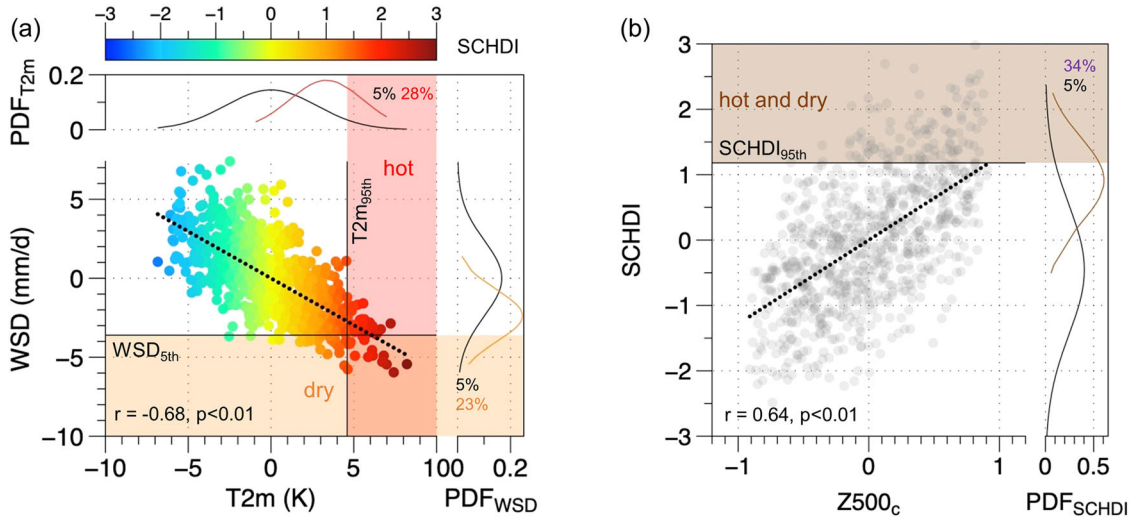

Fig. 3 | Distribution of T2m, WSD, and SCHDI, and their correlations to the atmospheric drivers. Scatter plots of **a** T2m and WSD anomalies and **b** $Z500_c$ anomalies and SCHDI. The dotted lines represent linear regressions of the respective samples. Marginal PDFs are derived for the entire summer (black solid curves), for T2m events when $Z500_T > Z500_{T,95th}$ (red solid curve), for WSD events when $Z500_W > Z500_{W,95th}$ (orange solid curve), and for SCHDI events when $Z500_c > Z500_{c,95th}$ (brown solid curve). The percentages quantify the frequency of T2m, WSD, and compound extremes for the whole summer (in black) and when $Z500_T > Z500_{T,95th}$ for T2m extremes (in red), when $Z500_W > Z500_{W,95th}$ for WSD extremes (in orange), and when $Z500_c > Z500_{c,95th}$ for compound events (in brown).

WSD in central Europe show a negative correlation of –0.68 ($p < 0.01$, 3a). The co-occurrence of low WSD and high T2m leads to compound hot and dry extremes, which is quantified by the Standardized Compound Hot and Dry Index (SCHDI, see Methods). The theoretical marginal distributions (normal distributions) reveal that the frequency of hot extremes increases from 5% (by definition) to 28% when only pentads with $Z500_T$ anomalies higher than the 95th percentile are considered. Similarly, during pentads characterized by $Z500_W > Z500_{W,95th}$, the frequency of dry extremes increases from 5% to 23% (Fig. 3a). Consistently, a positive correlation is evident between $Z500_c$ and SCHDI (Fig. 3b), with a linear regression slope of 0.64 ($p < 0.01$). The frequency of compound hot and dry extremes increases from 5% to 34% when $Z500_c > Z500_{c,95th}$. This is consistent with the atmospheric circulation coupling[36] driving the compound hot and dry extremes, i.e., a high pressure accompanied by less cloud and subsidence, which results in enhanced solar radiation and decreased precipitation[53].

Causal Effect Networks and hindcast models

To investigate the causal pathways linking T2m and WSD with their atmospheric precursors and surface drivers, we calculate the (CENs, see Methods) for single and compound hot and dry extremes (Fig. 4). When investigating single extremes, both $Z500_T$ and $Z500_W$ are used (Fig. 4a), while for compound extremes only $Z500_c$ is considered (Fig. 4b). We consider lags of –1, –2, and –3, which align with the typical occurrence of the precursor of hot/dry events, and we only show the significant causal links in the following analysis ($p < 0.05$). In the single extreme CEN (Fig. 4a), T2m has two significant causal parents at lag –1, $Z500_T$ ($Z500_T \rightarrow T2m$, $\beta = 0.35$, i.e., if $Z500_T$ increases by 1 standard deviation (s.d.) at lag –1, T2m will increase by 0.35 (s.d.) at lag 0) and WSD (WSD → T2m, $\beta = -0.18$). These two causal links can be interpreted respectively as (i) $Z500_T \rightarrow$ T2m: decreased cloud cover, which leads to increased solar radiation reaching the surface[53] and (ii) WSD → T2m: increased sensible heat flux due to suppressed evapotranspiration by limited soil moisture[54].

WSD shows three significant causal parents at lag –1: $Z500_W$ ($Z500_W \rightarrow WSD$, $\beta = -0.39$), T2m ($T2m \rightarrow WSD$, $\beta = 0.17$), and WSD itself ($WSD \rightarrow WSD$, $\beta = 0.16$). $Z500_W \rightarrow$ WSD is associated with high pressure and air subsidence, and therefore decreased precipitation[55]. T2m → WSD can be interpreted as a positive relationship between air temperature and moisture, according to the Clausius-Clapeyron scaling[56]. WSD → WSD indicates the soil moisture memory[57]. Notably, although $Z500_W$ and $Z500_T$ share a linear temporal correlation coefficient of 0.73 (see Table S1), distinct links from $Z500_T$ to T2m and from $Z500_W$ to WSD emphasize the necessity of considering these two atmospheric precursors separately.

Compared with single extremes, compound hot and dry events are characterized by two mechanisms, including the atmospheric coupling and the land-atmosphere interaction[36]. It is therefore critical to derive the CEN for compound extremes by taking into account $Z500_c$ instead of both $Z500_T$ and $Z500_W$. The peculiar feature of the compound CEN is that $Z500_c$ is identified as the causal parent of both T2m ($Z500_c \rightarrow T2m$, $\beta = 0.36$) and WSD ($Z500_c \rightarrow WSD$, $\beta = -0.34$)(Fig. 4b). This is motivated by the atmospheric coupling[36] which simultaneously leads to high solar radiation and low precipitation, and thus causes the co-occurrence of hot and dry extremes. The other links maintain the same directions as in the single extreme CEN, though with minor variations in the strength of the β values, including WSD → T2m ($\beta = -0.17$), T2m → WSD ($\beta = 0.27$), and WSD → WSD ($\beta = 0.22$).

Based on the drivers identified in the single extremes CEN (Fig. 4a), we hindcast the variations of T2m and WSD using a multivariate linear regression model. To assess the performance of models with different combinations of identified causal drivers we use the area under the receiver operating characteristic curve (AUC) score (for more details, see Methods), as shown in Fig. 4c–f. The hindcast model generally exhibits a higher AUC for hot and dry extremes compared to moderate conditions.

From the performance of the hindcast models, we notice that T2m variations are better predicted by $Z500_T$ than by WSD if a single driver is considered (see dotted lines in Fig. 4c). Indeed, the AUC score of the single-driver hindcast model ranges from 0.70 to 0.77 with $Z500_T$ and from 0.68 to 0.74 with WSD. However, the best hindcast is achieved when both $Z500_T$ and WSD are included (black solid line in Fig. 4c), with the AUC score ranging between 0.73 and 0.80. As for WSD variability, the AUC score of the single-driver hindcast model with $Z500_W$, WSD, and T2m range from 0.63 to 0.73, from 0.57 to 0.70, and 0.51 to 0.60, respectively (Fig. 4e). Panels 4c, e imply atmospheric precursors are more dominant for both T2m and WSD variability, and our precursors have a stronger hindcast power for T2m than WSD changes.

T2m and WSD variations are also hindcasted using causal drivers identified in the compound CEN (Fig. 4b), with the AUC scores shown in Fig. 4d, f. The results are generally consistent with the ones based on the single extreme CEN, with two major differences: (i) when hindcasting T2m,

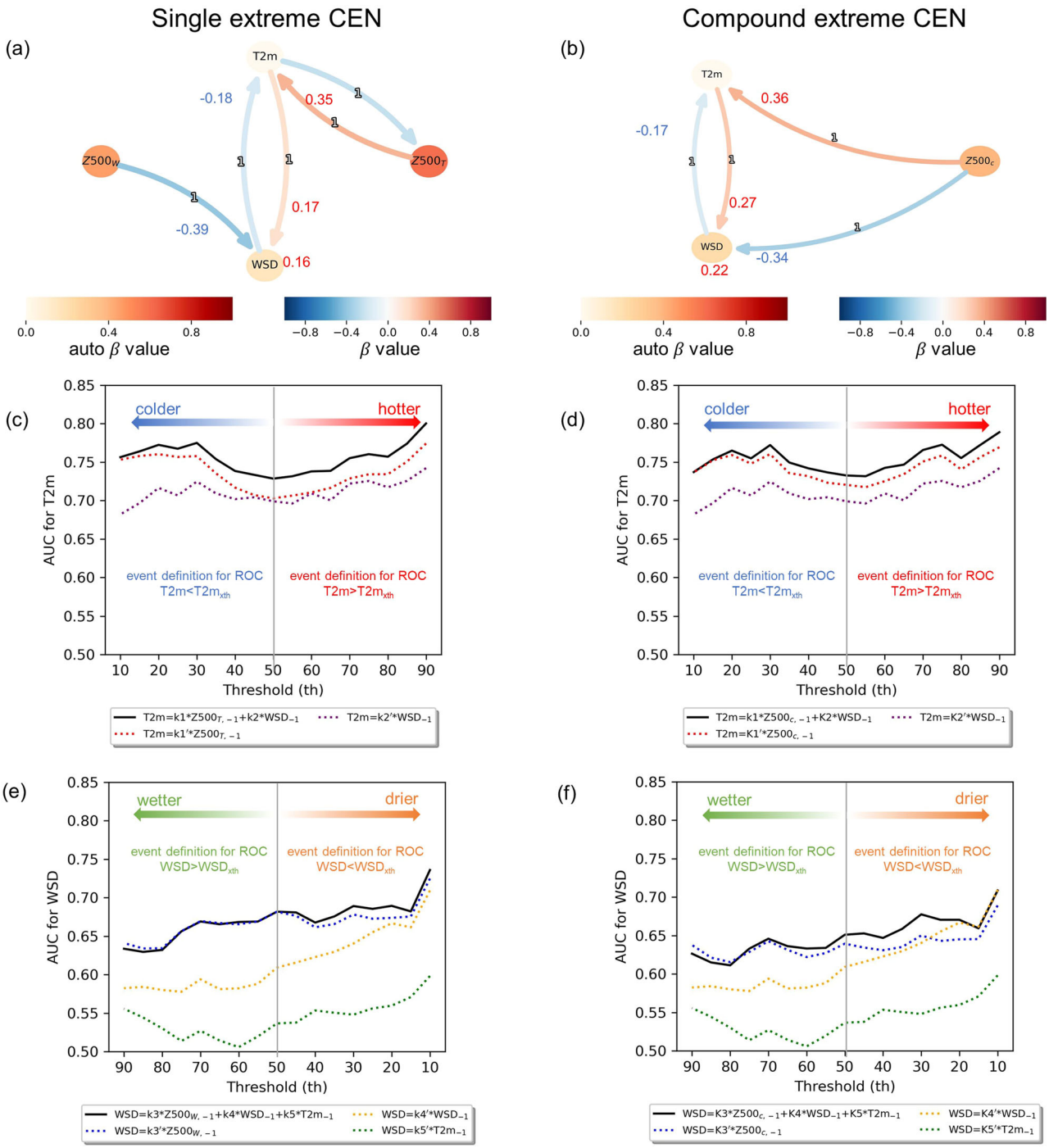

Fig. 4 | Single and compound extreme CENs and AUC scores of hindcast models. Left and right panels refer to single and compound extremes, respectively. **a**, **b** CENs with significant links; AUC scores for hindcasts of (**c**, **d**) T2m and (**e**, **f**) WSD based on the drivers identified in the single extreme CEN (**c**, **e**) and based on the drivers identified in the compound CEN (**d**, **f**). In (**c**–**f**), when threshold <50th, the event to compute the AUC score is defined as WSD < $WSD_{threshold}$ and T2m < $T2m_{threshold}$; when threshold ≥50th, the event to compute the AUC score is defined as WSD > $WSD_{threshold}$ and T2m > $T2m_{threshold}$. Solid lines represent the hindcast models based on all possible drivers, dotted lines represent the hindcast models based on single drivers. Note that the x-axis ranges from colder to hotter state in (**c**, **d**) and from wetter to drier state in (**e**, **f**).

the difference between the hindcast power of Z500 and WSD is larger in the compound case compared to the single case, especially for the middle quantiles (red and blue dotted lines in Fig. 4c, d); (ii) when hindcasting WSD, the hindcast power of WSD is higher than the atmospheric precursor if the dry extreme threshold is lower than the 30th percentile based on the compound extreme CEN (Fig. 4f), which is not seen in the single extreme one (Fig. 4e).

The interannual trend of causal links

Next, we analyze the historical trends of β values by calculating CENs using a 10-year moving window over the 1979–2020 period (see Fig. 5). The results show significant changes in T2m and WSD at the rate of 0.7 K per decade and −0.2 mm per day per decade, respectively, with the warming trend more intense than the drying trend (Fig. 5a). Moreover, the SCHDI has increased at the rate of 0.16 per decade (Fig. 5a). However, no significant trend is

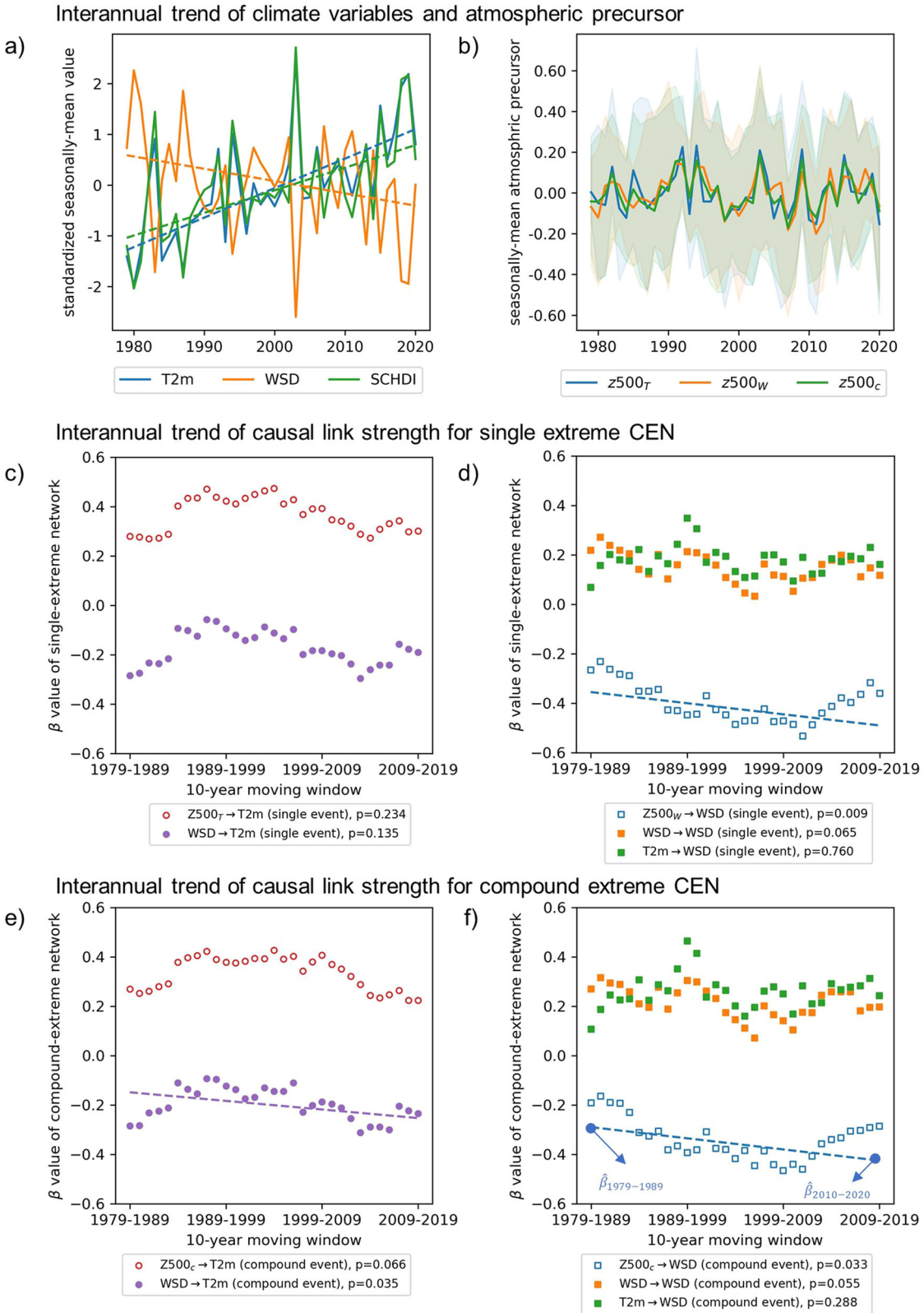

Fig. 5 | Interannual trends of climate variables, atmospheric drivers, and causal links strength. Interannual trends of **a** standardized summer seasonal-mean of T2m, WSD, and SCHDI and **b** atmospheric precursors. **c**–**f** Interannual trends of β values (**c**, **d**) for the single extreme CEN and (**e**, **f**) for the compound CEN. Solid lines in (**a**, **b**) represent year-mean values, dashed lines in (**a**–**f**) represent regressions with $p < 0.05$ and shadows in **b** cover the range from the seasonal 5th to the 95th percentiles. Circles and squares in (**c**–**f**) represent the causal links leading to T2m and WSD variations, respectively, while unfilled and filled scatters represent causal links where atmospheric precursors and land drivers are the causal drivers, respectively.

detected in the atmospheric precursors, nor in the median or in the extreme values (Fig. 5b). In contrast, an increasing strength (in absolute value) of some of the causal links (Fig. 5c–f) is evident. β values of $Z500_W \rightarrow WSD$ and $Z500_c \rightarrow WSD$ links present a decreasing trend of –0.05 per decade (Fig. 5d, f), while the β value of $WSD \rightarrow T2m$ shows a significant change at the rate of –0.03 per decade (Fig. 5e) in the compound CEN. Thus, we estimate the relative changes of the causal link strength for the analyzed period via

$$\frac{\hat{\beta}_{2010-2020} - \hat{\beta}_{1979-1989}}{\hat{\beta}_{1979-1989}}, \quad (1)$$

where $\hat{\beta}$ is the value of the causal strength estimated from the regression lines (see Fig. 5f). We find that the absolute impact of dry soil on temperature is amplified by 67% for the compound CEN ($\hat{\beta}^{WSD\rightarrow T2m}_{2010-2020} = -0.25$ and $\hat{\beta}^{WSD\rightarrow T2m}_{1979-1989} = -0.15$, see the purple dashed line of Fig. 5e), while the absolute influence of atmospheric drivers on soil moisture is intensified by 50% for compound CENs ($\hat{\beta}^{Z500_c\rightarrow WSD}_{2010-2020} = -0.42$ and $\hat{\beta}^{Z500_c\rightarrow WSD}_{1979-1989} = -0.28$, see the blue dashed line of Fig. 5f) and 36% for single CENs ($\hat{\beta}^{Z500_W\rightarrow WSD}_{2010-2020} = -0.49$ and $\hat{\beta}^{Z500_W\rightarrow WSD}_{1979-1989} = -0.36$, see the blue dashed line of Fig. 5d). This implies that the overall warmer and drier climate has a stronger impact on the causal links during compound hot and dry extremes than during single extremes.

We further perform three experiments to check how the background states of seasonal temperature and soil moisture content influence the strength of the causal links (Fig. 6). We construct CENs using sub-selections of 10 years based on increasing seasonal $T2m_{90th}$, decreasing seasonal WSD_{10th} and increasing seasonal $SCHDI_{90th}$ (see Supplementary material, Figs. S3a–c). A sensitive test shows that our results are robust to changes in the length of the sub-selection window (see Supplementary material, Supplementary note S2 and Figs. S4–S6). Here, we only focus on those links for which the influence of the background state is significant at $\alpha = 0.05$ and strong enough (absolute value of correlation coefficient between the causal link strength and corresponding climate variables (i.e., T2m, WSD, or SCHDI) > 0.7). The historical intensification of $Z500_W \rightarrow WSD$ link (Fig. 5) is related to soil water content decrease (Fig. 6d). The historical stronger $WSD \rightarrow T2m$ link (Fig. 5) can be attributed to both the warmer and drier background conditions (Fig. 6a, c, e).

While the aforementioned link variations are consistent with the ones detected in the observations, these experiments show that another causal link, namely $WSD \rightarrow WSD$, could undergo a potentially significant variation with higher temperature and lower soil moisture (Fig. 6b, d, f). In the single extreme CEN, the $WSD \rightarrow WSD$ link exhibits a positive correlation with $T2m_{90th}$ (linear regression coefficient equal to 0.10 per K) and a negative one with WSD_{10th} (linear regression coefficient equal to –0.071 per mm day^{-1}). In the compound CEN, the $WSD \rightarrow WSD$ link is amplified with increasing seasonal $SCHDI_{90th}$ (unitless) at the rate of 0.342 per 1 unit of seasonal $SCHDI_{90th}$ (Fig. 6f). The two changes in $WSD \rightarrow T2m$ and $WSD \rightarrow WSD$ suggest that WSD as a causal driver is the most affected by the seasonal background state.

The change in the strength of the causal link is more pronounced in the compound CEN compared to the single extreme one. Although the $WSD \rightarrow T2m$ link is amplified in both cases, its β value exceeds the 10% significance test confidence bounds (purple shadows) (Fig. 6e) only in the compound CEN. For high values of the seasonal $SCHDI_{90th}$, the $WSD \rightarrow T2m$ link reaches twice its average value computed from the entire 42 years set (Fig. 6e), which is not observed with varying $T2m_{90th}$ (Fig. 6a) and WSD_{10th} (Fig. 6b). This further distinguishes the compound extremes case from the single one apart from the atmospheric circulation coupling: T2m and WSD co-vary more strongly when the background state is both warmer and drier.

SST patterns favoring hot and dry conditions in central Europe

Previous literature has associated the "Atlantic low-Europe high" pattern depicted in Fig. 2a (lag –1 and lag 0) with sea surface temperature (SST) anomalies in the North Atlantic[58], which motivates us to investigate the related variations in SST. The composite of SST anomalies for the 10 years with the highest seasonal-mean $Z500_T$ shows a positive anomaly over western North America, central Europe, and central northern Siberia, with negative anomalies over North Pacific, eastern North America, North Atlantic, and eastern Europe (Fig. 7d). Furthermore, the low-pressure system over the mid-latitude North Atlantic associated with high $Z500_T$ deepens over Greenland, which resembles a negative phase of the NAO (Fig. 7b). The composite for the highest 10 seasonal $Z500_W$ is similar to the $Z500_T$ pattern, although we notice a more pronounced positive center over central Europe, a high-pressure system to the south of the Atlantic low, and generally negative Z500 anomalies in the Arctic (Fig. 7c).

The corresponding SST anomaly in Fig. 7d, e reveals both similarities and differences. During years with high seasonal mean $Z500_T$, significant negative SST anomalies can be observed in the mid- and high-latitude North Atlantic, with positive anomalies occurring in the subtropics and negative anomalies over the tropical North Atlantic (Fig. 7d). To quantify this relationship, we calculate the yearly summer-mean SST in midlatitude North Atlantic (45°–20° W, 45°–15° N[58], shown in Fig. 7a as $SST_{Atlantic}$). We found that yearly summer-mean $SST_{Atlantic}$ is significantly correlated with $Z500_T$ ($r = -0.63$, $p < 0.01$) and $Z500_W$ ($r = -0.44$, $p < 0.01$). In addition, warm anomalies occur over the North Pacific, from the northeastern part of the North Pacific towards the eastern and central tropical Pacific, while cold anomalies cover the western tropical Pacific. Similarly, during years with high seasonal mean $Z500_W$, we observe a southward cold-warm-cold SST pattern over the North Atlantic and a warmer eastern Pacific Ocean (Fig. 7e). However, cold anomalies over the tropical Atlantic in Fig. 7e are not as significant as the ones in Fig. 7d.

Furthermore, we investigate the influence of the $SST_{Atlantic}$ on the single and compound extreme CENs by using sub-selections of 10 years based on increasing seasonal-mean $SST_{Atlantic}$. As shown in Fig. S7, colder Atlantic SSTs have a similar impact on the single extreme CEN (Fig. S7a, S7b) as warmer temperatures in central Europe (Fig. 6a, b), especially regarding to $WSD \rightarrow T2m$ and $WSD \rightarrow WSD$. However, Atlantic SSTs do not significantly affect the compound extreme CENs (Fig. S7c, S7d).

Discussion

In this study, we link single and compound hot and dry extremes in central Europe to their large-scale atmospheric precursors and local surface drivers and quantify the causal pathways based on the PCMCI causal algorithm. Our analysis reveals that ten days before hot and dry extreme events, a distinct atmospheric configuration characterized by a high-pressure system over the CEU and a concomitant low-pressure system in the western North Atlantic emerges, which then becomes significant five days before the occurrences of extremes (Fig. 2). This atmospheric pattern can be further correlated to a zonal cold-warm-cold SST pattern across the North Atlantic and warmer temperatures in the eastern North Pacific (Fig. 7). Notably, when these atmospheric precursors exceed their 95th percentile, the likelihood of single hot, single dry, and compound extremes show a 6-, 5-, and 7-fold increase, respectively (Fig. 3).

The CEN analysis shows that the intra-seasonal T2m variability is influenced by both the atmospheric pattern ($Z500_T \rightarrow T2m$, AUC ≈ 0.70–0.77) and the WSD ($WSD \rightarrow T2m$, AUC ≈ 0.68–0.74). Similarly, the WSD variability is also predominantly governed by its atmospheric precursor ($Z500_W \rightarrow WSD$, AUC ≈ 0.63–0.73), while changes in its own dynamics ($WSD \rightarrow WSD$, AUC ≈ 0.57–0.70) and temperature anomalies ($T2m \rightarrow WSD$, AUC ≈ 0.51–0.60) show a weaker causal effect (Fig. 4). Moreover, under warming and drying trends, WSD results as the most affected variable: its causal effect on the other actors increases ($WSD \rightarrow T2m$ and $WSD \rightarrow WSD$), while becoming more sensitive to changes of its causal precursors ($Z500_W \rightarrow WSD$, Figs. 5 and 6).

By building and comparing CENs for the single and compound extremes separately, we show that compound hot and dry events are the

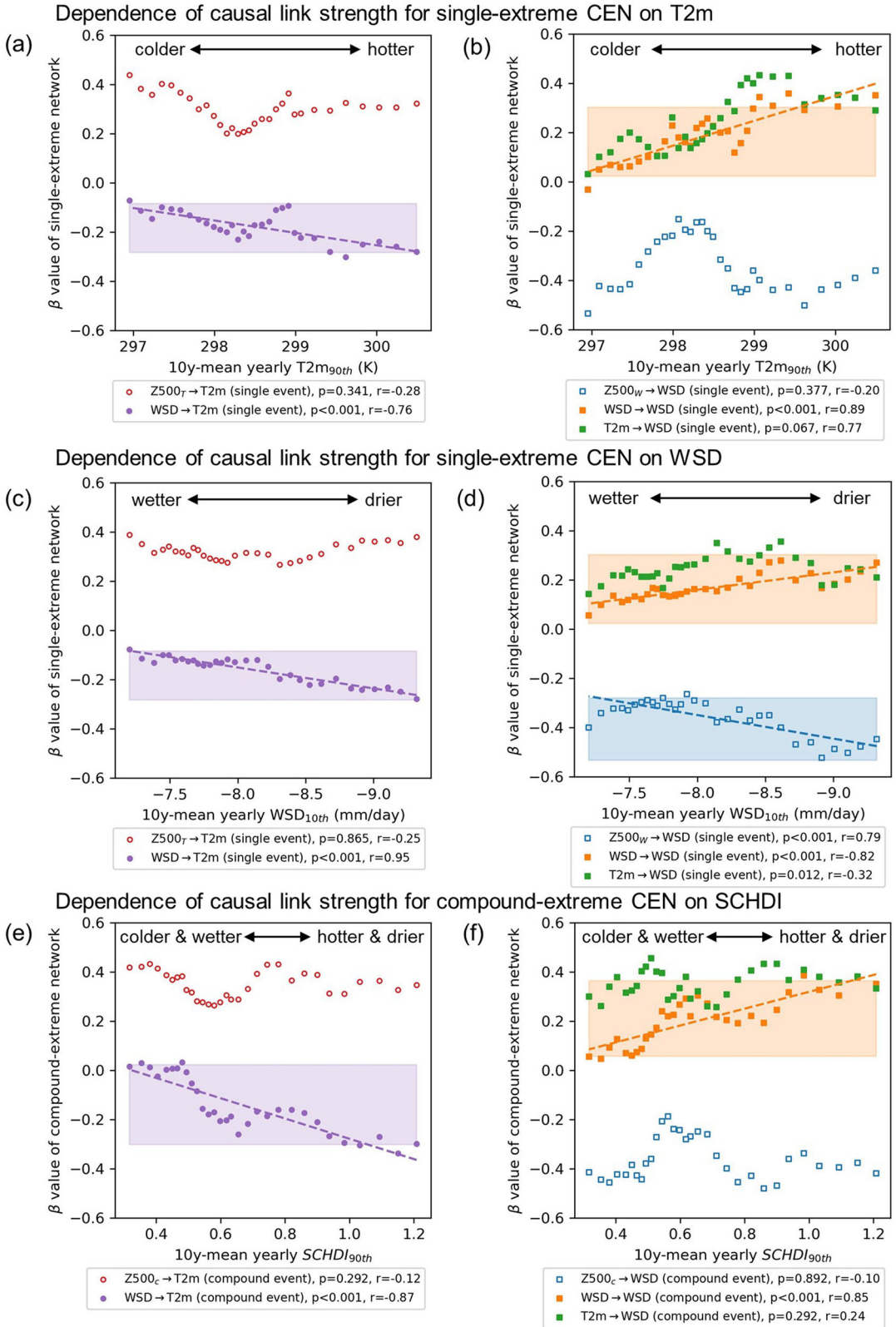

Fig. 6 | Variation of causal links with T2m and WSD conditions. Changes of β values in (**a**–**d**) single extreme and (**e, f**) compound CENs. Each β value is calculated using 10 years moving window according to (**a**, **b**) increasing seasonal $T2m_{90th}$, (**c**, **d**) decreasing seasonal WSD_{10th}, and (**e, f**) increasing seasonal $SCHDI_{90th}$. 10% confidence bounds (shadows) are computed by calculating 1000 surrogates β values from bootstrapped sets of 10 years. The shown linear regressions (dashed lines) are significant at $\alpha = 0.05$ and are characterized by a correlation coefficient between β value and corresponding climate variables (i.e., T2m, WSD, or SCHDI) > 0.7. Circles and squares represent the causal links leading to T2m and WSD, respectively, while unfilled and filled scatters represent causal links where atmospheric precursors and land drivers are the causal drivers, respectively. Notice that the *x*-axis ranges from colder to hotter state in (**a**, **b**), from wetter to drier state in (**c**, **d**), and from colder/wetter to hotter/drier state in (**e**, **f**).

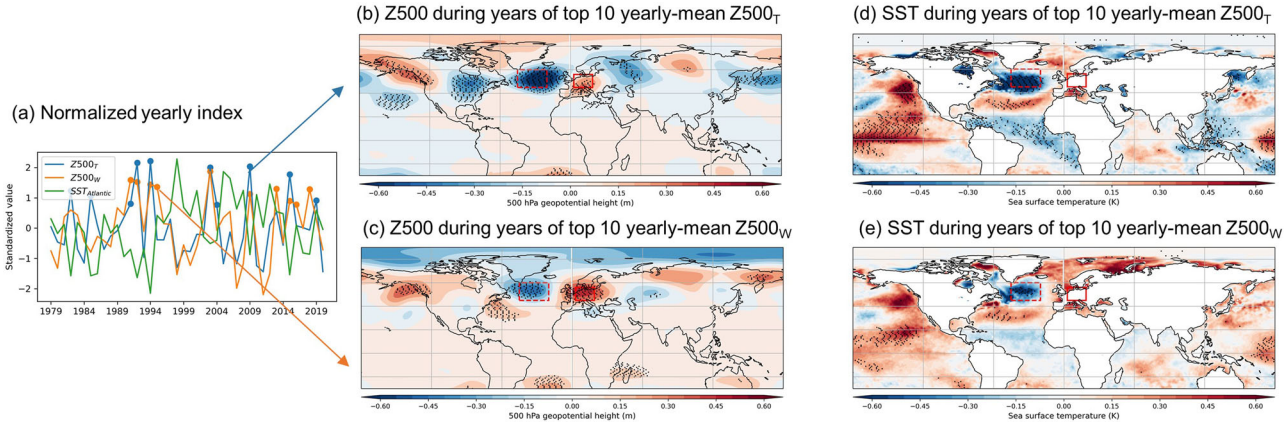

Fig. 7 | Large-scale atmospheric patterns and sea surface temperature. **a** Standsardized seasonal-mean $Z500_T$, $Z500_W$, and the Atlantic-mean SST anomaly. Dots representing the top 10 years of corresponding time series. The Atlantic region is indicated by the dashed red box in (**b**–**e**). Z500 anomaly composites during top 10 years of **b** $Z500_T$ and **c** $Z500_W$ seasonal mean. SST anomaly composites during top 10 years of **d** $Z500_T$ and **e** $Z500_W$ seasonal mean. In (**b**–**e**), black dots represent grid points where the anomaly is significant at $\alpha = 0.05$, solid red box refers to central Europe, dashed red box refers to the region in the North Atlantic Ocean that is related to CEU hot and dry extremes.

result of (i) amplified atmospheric coupling, which is indicated by the causal effect of atmospheric precursor on both T2m and WSD in the compound CEN (Fig. 4a, b) and (ii) intensified land-atmosphere interactions, revealed by a stronger and more significant intensification of the WSD → T2m link with high SCHDI than with single extremes indices (Figs. 5, 6). While being in accordance with prior studies[36,59–61], here we are able to quantify the differences between the causal links in single and compound CENs. During 1979–2020, the strength of the WSD → T2m link is amplified by 67% for compound CEN (Fig. 5e), and the strength of $Z500_c$ → WSD ($Z500_W$ → WSD) increases by 50% (36%) for compound (single) CEN (Fig. 5d, f). Moreover, although the warming or drying conditions intensify the land-atmosphere interactions when separately analyzed (Fig. 6a, c), the strength of the WSD → T2m link reaches twice its average value under the co-occurrence of hot and dry conditions (Fig. 6e). Thus, our findings help to explain the more pronounced increase of compound extremes[37].

Previous studies attempted to decompose the warming trend in Europe into its dynamic[62] and thermodynamic components[63]. The dynamic part refers to whether the frequency or intensity of atmospheric circulation is conducive to hot and dry extremes, while the thermodynamic one represents whether the forcing of the atmospheric or surface drivers get strengthened due to warming. To distinguish their relative importance, earlier studies have employed quantile-regression analysis between T2m and circulation features[62,64] to calculate the dynamic changes and then interpret the residual as thermodynamic changes. However, the quantile regression does not allow a quantitative causal analysis. In our study, we apply CENs to directly assess the thermodynamic forcing by analyzing the changes in the causal links. Our results provide statistical evidence for the key role of the thermodynamic drivers, which is evidenced by the variations in the strength of the causal links (Figs. 5, 6).

Europe has been affected by hot and dry extremes at an enhanced pace compared to other northern mid-latitude regions, with a rise of ~0.61 days per decade[5] and a significant increase in flash droughts occurrences by up to 80%[65]. Our findings are in line with these studies and provide deeper insights into global warming influence on the occurrence of hot and dry extremes. Generally, both T2m variability and WSD changes are more sensitive to their atmospheric precursor (Fig. 8a). By analyzing the historical trends (Fig. 5), we observe three ways leading to a warmer and drier climate, through (i) the stronger strength of causal drivers, (ii) the enhanced strength of causal links, and (iii) the intensified strength of both causal drivers and causal links (Fig. 8a). The latter two scenarios pose an extra risk to the hot and dry extreme effects due to their nonlinear nature. For instance, T2m increases if soil moisture decreases ($T2m \propto \beta_T^2 \times WSD$), and thus the overall drying trend directly affects temperature even considering a constant β_T^2. However, we show that β_T^2 has been intensifying over the last decades as well, from which the nonlinear effect on T2m due to the simultaneous variations of both WSD and β_T^2.

Under warming or drying trend, three causal links are significantly intensified (Fig. 8b), including WSD → T2m (β_T^2), $Z500_W$ → WSD (β_W^1), and WSD → WSD (β_W^3). The heightened response of WSD → T2m (β_T^2) under hot and dry conditions is associated with reduced evapotranspiration due to limited soil moisture, leading to increased sensible heat flux[66]. The increasing strength of $Z500_W$ → WSD (β_W^1) causal link can be explained by an enhanced hydrological cycle and an increasing concurrence of soil drought and atmospheric aridity due to land-atmosphere interaction. Once high pressure leads to reduced precipitation, the WSD will quickly respond due to the overall soil moisture shortage[67]. The sensitivity of WSD → WSD (β_W^3) to temperature, rarely reported before, can be comprehended within the context of soil moisture-limited regime[68]. In this scenario, a positive feedback loop initiated by a deficit in soil moisture causes a reduction in evaporation. This consequently causes a temperature increase, leading to a decreased cloud cover and precipitation, ultimately resulting in a further decline in soil moisture.

Global warming will further add to these nonlinear effects, especially for compound events. On the one hand, historical observations already show a stronger increase in the causal pathways of compound CEN compared to the single extreme CEN (β_W^1 and β_T^2, Fig. 8b). On the other hand, we show that under a warmer and drier climate soil moisture memory could increase (β_W^3, Fig. 8b), and indeed some studies have already reported a continuous warming temperature and drying soil in central Europe and over larger areas[69,70]. These spatio-temporal variations in temperature and soil moisture imply further changes in the causal links, especially under different emission scenarios. Further research is needed to quantify the risks based on future climate projections and to assess the CEN of hot and dry extremes with other human-related drivers included to disentangle the anthropogenic contribution from the natural variability.

Methods

Data

In this study, we focus on hot and dry extremes located in central Europe, defined as the continental region between 45°N –55°N, 3°E–18°E (Fig. 1). We analyze daily data from the ERA5 reanalysis dataset[52] with a spatial resolution of 1° × 1° for summer (June, July, August, JJA) during the 1979–2020 period, including 2 m temperature (T2m), 500-hPa geopotential height (Z500), precipitation (Pr), potential evapotranspiration (PET), and sea surface temperature (SST). All mentioned fields are detrended and anomalies are calculated at pentads (5-day averages) time steps, thus removing the climatological cycles.

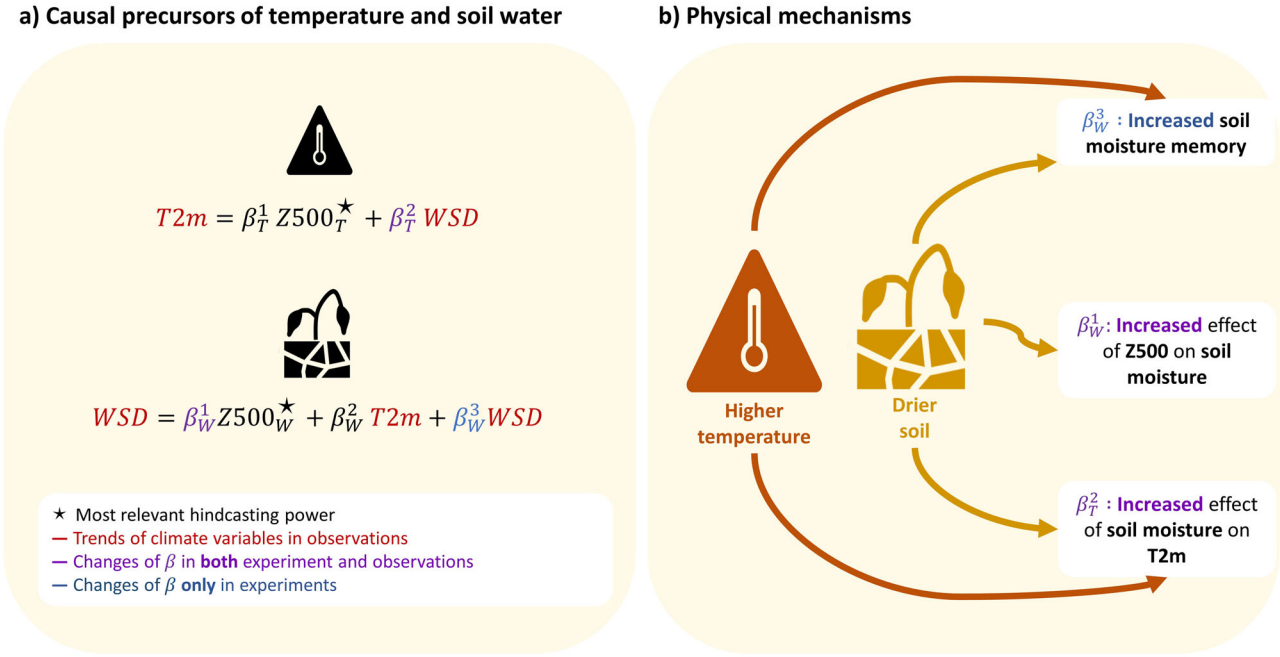

Fig. 8 | Schematic summary. a Linear hindcast model of T2m and WSD based on causal drivers and the changes in the Causal Effect Networks. **b** Physical mechanisms highlighted by our causal analysis.

T2m is selected as a local variable to assess hot conditions, while the WSD as a local indicator of wet/dry conditions. The WSD is expressed in millimeters per day (mm d^{-1}) and defined as the difference between cumulated Pr and PET for a given location i and period t[71]:

$$\mathrm{WSD}(i,t) = \mathrm{Pr}(i,t) - \mathrm{PET}(i,t). \quad (2)$$

Standardized compound hot and dry index

To analyze hot and dry compound extremes, we consider the SCHDI. The SCHDI is calculated following Li et al.[71] using T2m and WSD as variables:

$$\mathrm{SCHDI}_i = \Phi^{-1}\left(F\left(\mathbb{P}\left(\mathrm{T2m} \geq \mathrm{T2m}_i, \mathrm{WSD} \leq \mathrm{WSD}_i\right)\right)\right), \quad (3)$$

where Φ^{-1} is the inverse of the standard normal distribution and F is the marginal cumulative distribution of the variable $T = \mathbb{P}\left(\mathrm{T2m} \geq \mathrm{T2m}_i, \mathrm{WSD} \leq \mathrm{WSD}_i\right)$, i.e., $F = P(T \leq t)$, to remap the joint probability $\mathbb{P}$ into the uniform distribution in [0, 1]. $\mathrm{T2m}_i$ and WSD_i are T2m and WSD on timestamp i.

We evaluate the association between T2m and WSD using Kendall's τ, checking its statistical significance. Then, we used BiCopSelect, an R function to select the optimal copula function based on the Akaike Information Criterion (AIC), which allows us to calculate the joint cumulative distribution of T2m and WSD. The BiCopSelect function includes 37 potential bivariate copulas, including Gaussian, Student-t copula, Clayton, Gumbel, Frank, Joe, BB1, BB6, BB7, BB8 copulas, as well as the rotated versions of Clayon, Joe, Gumbel, BB1, BB6, BB7, BB8 copulas (10.32614/CRAN.-package.VineCopula). Among these families, the Gaussian copula (with $par = -0.68$) is the best fit for our data, which is further validated by the Cramér-von Mises (CvM) goodness of fit (GOF) test. We obtain $CvM_{p-value} = 0.89$ and $CvM_{statistic} = 0.06$. This supports our choice of Gaussian copula to calculate the SCHDI.

Next, we calculate empirically the distribution F (which corresponds to the Kendall distribution function when the variable considered is $\mathbb{P}\left(\mathrm{T2m} \leq \mathrm{T2m}_i, \mathrm{WSD} \leq \mathrm{WSD}_i\right)$) to ensure that the joint cumulative distribution is uniformly distributed within the range [0, 1][72,73]. Finally, we calculate the inverse of the standard normal distribution to obtain the SCHDI.

Definition of extremes and the impact of atmospheric precursors

We define a hot extreme as an event occurring at time t when

$$\mathrm{T2m}(t) \geq \mathrm{T2m}_{95\mathrm{th}}, \quad (4)$$

where $\mathrm{T2m}_{95\mathrm{th}}$ is the 95th percentile of T2m anomaly. A dry extreme occurs whenever

$$\mathrm{WSD}(t) \leq \mathrm{WSD}_{5\mathrm{th}}, \quad (5)$$

with $\mathrm{WSD}_{5\mathrm{th}}$ the 5th percentile of WSD anomaly. A compound event is detected at t if both conditions defined by Eqs. (4) and (5) hold.

Based on the previous definitions, we build Z500 composite fields for T2m, WSD, and compound extremes at different lags (see Fig. 2). Focusing on a region corresponding to three ridge-trough pairs, we construct precursors time series by computing the linear correlation between the composite field at lag −1 and the Z500 field at each time step. This is done for each of the three composites, obtaining the Z500 precursor time series for T2m extremes ($Z500_T$), WSD extremes ($Z500_W$), and compound extremes ($Z500c$).

To analyze the influence of atmospheric precursors on the occurrence of weather extremes, the marginal distributions of T2m, WSD, and SCHDI are calculated for both the entire JJA period and for time steps where the atmospheric precursor is amplified, i.e., $Z500_T > Z500_{T,90th}$, $Z500_W > Z500_{W,90th}$, and $Z500_c > Z500_{c,90th}$ (see Fig. 3).

PCMCI causal discovery algorithm

The PCMCI algorithm is a two-step causal discovery tool that allows to distinguish between causal and spurious dependences among a set of time series, here defined as actors[74,75]. PCMCI considers a time lag among actors, thus detecting the causal influence of one actor on others at a later point in time. PCMCI relies on several assumptions, such as (i) causal sufficiency, (ii) causal stationarity, (iii) the absence of instantaneous causal effects from one variable to another, (iv) the causal Markov condition, and (v) the faithfulness[46].

Given a set of N actors, we call X_i^t the realization at time t of variable X_i. The objective is to find a set of causal parents $\mathcal{P}$ for each actor X_i^t:

$$\mathcal{P}(X_i^t) := \{X_j^{t-\tau} : X_j \in \mathcal{X}, \tau > 0, X_j^{t-\tau} \to X_i^t\} \text{ for } i, j = 1, 2, ..., N, \quad (6)$$

where $\mathcal{X}$ is the set of actors, τ is a certain lag and $X_j^{t-\tau} \to X_i^t$ indicates the direct causation (link) from $X_j^{t-\tau}$ to X_i^t. Two actors X_i^t and $X_j^{t-\tau}$ are connected by a direct link if and only if

$$X_j^{t-\tau} \not\perp\!\!\!\perp X_i^t | \mathcal{X} \setminus \{X_j^{t-\tau}\}, \quad (7)$$

which reads X_i^t and $X_j^{t-\tau}$ are not conditionally independent given the set of actors $\mathcal{X}$ minus $X_j^{t-\tau}$.

The set of parents is determined via iterative independence testing among the actors, using a test statistic of choice and analyzing different time lags. In this study, we use partial correlation, a regression-based test statistic, assuming near-linear interactions between actors at least in a first-order approximation. We focus on lags −1, −2, and −3, covering a period of up to 15 days and show significant causal links ($p < 0.05$).

The PC step is a condition selection stage designed to identify a provisional set of causal parents $\hat{\mathcal{P}}(X_i^t)$ for every X_i^t at a certain significance threshold α. It works as follows:

1. it checks if the unconditional cross correlation $\rho(X_j^{t-\tau}; X_i^t)$ is significant, for every considered lag τ and pair i, j;
2. if so, it checks if the conditional cross correlation with one condition $\rho(X_j^{t-\tau}; X_i^t | X_i^{t-1})$ is significant, where only the actor with the strongest absolute correlation with X_i^t is used[75];
3. step 2 is repeated by increasing the number of conditions, until the number of possible causal parents is equal to or smaller than the number of conditions needed to calculate the next partial correlation; if the partial correlation between actors X_i^t and $X_j^{t-\tau}$ is still significant, $X_j^{t-\tau}$ is identified as a provisional parent of X_i^t: $X_j^{t-\tau} \in \hat{\mathcal{P}}(X_i^t)$.

At the end of the PC step, each actor has its own set of provisional parents. The objective of the MCI stage is to get the definitive set of parents for each actor. This is done by verifying whether an actor and each of its provisional parents are still not conditionally independent given both their set of parents:

$$X_j^{t-\tau} \not\perp\!\!\!\perp X_i^t | \mathcal{P}(X_i^t) \setminus \{X_j^{t-\tau}\}, \mathcal{P}(X_j^{t-\tau}). \quad (8)$$

The significance of the causal link is based on the p-values of the MCI test. To take into account multiple significance testing, the Benjamini-Hochberg false discovery rate approach[76,77] is used to correct the p-values. To perform PCMCI the Python package Tigramite version 5.0 is used (https://github.com/jakobrunge/tigramite).

The analysis results in a CEN, an object composed of nodes representing each actor, and links, directed from the parent to the actor, weighted by the strength of the causal interaction and specific to the lag τ at which the interaction occurs. The weight of the causal link $X_j^{t-\tau} \to X_i^t$, i.e., the causal link strength, which we call β value, represents the expected change in X_i in s.d. units at time t when X_j gets perturbed at time $t-\tau$ by one s.d.[78].

Statistical hindcast model based on causal precursors

We use the set of identified causal parents to build hindcast models of T2m and WSD by applying multivariate linear regression. Next, we calculate the Area Under the Curve (AUC) score to test the performance of the hindcast models.

The AUC score is an index derived from the receiver operating characteristic (ROC) curve, a graphical representation to illustrate the performance of a binary classifier model across various threshold values[79]. For different threshold settings on a predefined set of observed events, true and false positive rates (i.e., the number of correctly and wrongly predicted events, respectively) are computed from the predicted time series and used to build the ROC curve. The AUC is a commonly used metric to evaluate model predictions in climate science[80]. An AUC = 1.0 indicates perfect predictive skill, while an AUC ≤ 0.5 means no skill.

To avoid overfitting, we use a fivefold cross-validation test. Fivefold cross-validation means that the dataset is split into five equal-sized (or as close to equal as possible) subsets. The hindcast model is trained on four of these subsets (training set) but only validated with the remaining one (testing set), based on the AUC score. In this way, every individual data is incorporated into four various training sets and used once as the validation set, which ensures our evaluation accurately reflects the model's performance on previously unseen data.

Bootstrapping and significance

To analyze the sensitivity of the strength of the β values to the occurrence of hot, dry, and compound extremes in CEU, we construct multiple CENs for different time windows, going from periods characterized by more intense events to less intense ones. The length of the time window is set to 10 JJA seasons, in order to have enough data for statistical representativeness of the resulting running time series. Thus, consecutive groups of 10 summer seasons (i.e., 33 intervals in the 42 years 1979 to 2020) are unambiguously ranked according to the three extreme scenarios, via the 90th percentile of T2m, the 10th percentile of WSD and the 90th percentile of the SCHDI. This way, we can construct 33 different CENs for each of the three scenarios and, subsequently, assess for each link the β value change going from more extreme to less extreme time periods. The significance of the computed links strength is evaluated by calculating 1000 surrogates of β value obtained by randomly subselecting 10 JJA seasons out of the 42 considered years and checking if the obtained value lies outside the 90% confidence interval (two-sided test).

Considering that the time series obtained by the 10 JJA seasons moving window are not independent of one from the other, the significance test should be based on the shuffle of independent blocks of 10 seasons[81]. However, this shuffling would only result in ~4 sets of surrogate series, which is insufficient to perform the significance test. Therefore, we also use blocks of 7 and 5 seasons to perform the shuffle, producing 1000 surrogates.

Reporting summary

Further information on research design is available in the Nature Portfolio Reporting Summary linked to this article.

Data availability

Data presented in this manuscript are available through the Copernicus Climate Change Service Climate Data Store (CDS, https://doi.org/10.24381/cds.adbb2d47 and https://doi.org/10.24381/cds.bd0915c6) for ERA5 reanalysis data.

Code availability

All the codes for analysis are available via https://github.com/tiany97/CEU_CEN. All analyzes were done in R (v.4.3.1) and Python (v.3.9.18) with Package Tigramite (v.5.1.0.3).

Received: 24 May 2024; Accepted: 26 November 2024;
Published online: 12 December 2024

References

1. Copernicus. Copernicus: 2023 is the hottest year on record, with global temperatures close to the 1.5°C limit. https://climate.copernicus.eu/copernicus-2023-hottest-year-record (accessed 11 September 2024) (2024).
2. Copernicus. European summer 2023: a season of contrasting extremes. https://climate.copernicus.eu/european-summer-2023-season-contrasting-extremes (accessed: 11 September 2024) (2023).
3. Baldwin, J. W., Dessy, J. B., Vecchi, G. A. & Oppenheimer, M. Temporally compound heat wave events and global warming: an emerging hazard. *Earth's Future* **7**, 411–427 (2019).

4. WMO. Atlas of Mortality and Economic Losses from Weather, Climate and Water Extremes (1970–2019). *WMO-No. 1267* (WMO, 2021).
5. Rousi, E., Kornhuber, K., Beobide-Arsuaga, G., Luo, F. & Coumou, D. Accelerated western European heatwave trends linked to more-persistent double jets over Eurasia. *Nat. Commun.* **13**, 3851 (2022).
6. Zschenderlein, P., Fink, A. H., Pfahl, S. & Wernli, H. Processes determining heat waves across different European climates. *Q. J. R. Meteorol. Soc.* **145**, 2973–2989 (2019).
7. Röthlisberger, M. & Papritz, L. Quantifying the physical processes leading to atmospheric hot extremes at a global scale. *Nat. Geosci.* **16**, 210–216 (2023).
8. White, R. H., Kornhuber, K., Martius, O. & Wirth, V. From atmospheric waves to heatwaves: a waveguide perspective for understanding and predicting concurrent, persistent, and extreme extratropical weather. *Bull. Am. Meteorol. Soc.* **103**, E923–E935 (2022).
9. Robinson, A., Lehmann, J., Barriopedro, D., Rahmstorf, S. & Coumou, D. Increasing heat and rainfall extremes now far outside the historical climate. *npj Clim. Atmos. Sci.* **4**, 45 (2021).
10. Lehmann, J., Coumou, D. & Frieler, K. Increased record-breaking precipitation events under global warming. *Climatic Change* **132**, 501–515 (2015).
11. Vogel, M. M., Zscheischler, J. & Seneviratne, S. I. Varying soil moisture–atmosphere feedbacks explain divergent temperature extremes and precipitation projections in central Europe. *Earth Syst. Dyn.* **9**, 1107–1125 (2018).
12. Miralles, D. G., Teuling, A. J., Van Heerwaarden, C. C. & Vilà-Guerau de Arellano, J. Mega-heatwave temperatures due to combined soil desiccation and atmospheric heat accumulation. *Nat. Geosci.* **7**, 345–349 (2014).
13. Copernicus. Precipitation, relative humidity and soil moisture for August 2023. https://climate.copernicus.eu/precipitation-relative-humidity-and-soil-moisture-august-2023 (accessed 11 September 2024) (2023).
14. Seneviratne, S. I. et al. Changes in climate extremes and their impacts on the natural physical environment. In Field, C. B. et al. (eds.) *Managing the Risks of Extreme Events and Disasters to Advance Climate Change Adaptation*, 109–230 (Cambridge University Press, 2012).
15. Wilhite, D. A. & Glantz, M. H. Understanding: the drought phenomenon: the role of definitions. *Water Int.* **10**, 111–120 (1985).
16. Spinoni, J. et al. Future global meteorological drought hot spots: a study based on CORDEX data. *J. Clim.* **33**, 3635–3661 (2020).
17. Cook, B. I., Mankin, J. S. & Anchukaitis, K. J. Climate change and drought: from past to future. *Curr. Clim. Change Rep.* **4**, 164–179 (2018).
18. Spinoni, J., Naumann, G., Vogt, J. V. & Barbosa, P. The biggest drought events in Europe from 1950 to 2012. *J. Hydrol. Reg. Stud.* **3**, 509–524 (2015).
19. Otkin, J. A. et al. Flash droughts: a review and assessment of the challenges imposed by rapid-onset droughts in the United States. *Bull. Am. Meteorol. Soc.* **99**, 911–919 (2018).
20. Hoerling, M. et al. Causes and predictability of the 2012 Great Plains drought. *Bull. Am. Meteorol. Soc.* **95**, 269–282 (2014).
21. Yuan, X., Wang, L. & Wood, E. F. et al. Anthropogenic intensification of Southern African flash droughts as exemplified by the 2015/16 season. *Bull. Am. Meteorol. Soc.* **99**, S86–S90 (2018).
22. Wang, L., Yuan, X., Xie, Z., Wu, P. & Li, Y. Increasing flash droughts over China during the recent global warming hiatus. *Sci. Rep.* **6**, 30571 (2016).
23. Mo, K. C. & Lettenmaier, D. P. Prediction of flash droughts over the United States. *J. Hydrometeorol.* **21**, 1793–1810 (2020).
24. Mo, K. C. & Lettenmaier, D. P. Heat wave flash droughts in decline. *Geophys. Res. Lett.* **42**, 2823–2829 (2015).
25. Christian, J. I. et al. Global distribution, trends, and drivers of flash drought occurrence. *Nat. Commun.* **12**, 6330 (2021).
26. Russo, S., Sillmann, J. & Fischer, E. M. Top ten European heatwaves since 1950 and their occurrence in the coming decades. *Environ. Res. Lett.* **10**, 124003 (2015).
27. Perkins, S. E. & Alexander, L. V. On the measurement of heat waves. *J. Clim.* **26**, 4500–4517 (2013).
28. Bevacqua, E., Zappa, G., Lehner, F. & Zscheischler, J. Precipitation trends determine future occurrences of compound hot-dry events. *Nat. Clim. Change* **12**, 350–355 (2022).
29. Ionita, M., Caldarescu, D. E. & Nagavciuc, V. Compound hot and dry events in Europe: variability and large-scale drivers. *Front. Clim.* **3**, 1–19 (2021).
30. Zscheischler, J. et al. A typology of compound weather and climate events. *Nat. Rev. Earth Environ.* **1**, 333–347 (2020).
31. Mukherjee, S., Mishra, A. K., Zscheischler, J. & Entekhabi, D. Interaction between dry and hot extremes at a global scale using a cascade modeling framework. *Nat. Commun.* **14**, 1–15 (2023).
32. Vogel, M. M., Zscheischler, J., Wartenburger, R., Dee, D. & Seneviratne, S. I. Concurrent 2018 hot extremes across Northern Hemisphere due to human-induced climate change. *Earth's Future* **7**, 692–703 (2019).
33. IPCC. *Climate Change 2022 - Impacts, Adaptation and Vulnerability: Working Group II Contribution to the Sixth Assessment Report of the Intergovernmental Panel on Climate Change* (Cambridge University Press, 2023).
34. Tripathy, K. P., Mukherjee, S., Mishra, A. K., Mann, M. E. & Williams, A. P. Climate change will accelerate the high-end risk of compound drought and heatwave events. *Proc. Natl. Acad. Sci.* **120**, 2017 (2023).
35. Kautz, L.-A. et al. Atmospheric blocking and weather extremes over the Euro-Atlantic sector—a review. *Weather Clim. Dyn.* **3**, 305–336 (2022).
36. Lesk, C. et al. Stronger temperature–moisture couplings exacerbate the impact of climate warming on global crop yields. *Nat. Food* **2**, 683–691 (2021).
37. Zscheischler, J. & Seneviratne, S. I. Dependence of drivers affects risks associated with compound events. *Sci. Adv.* **3**, e1700263 (2017).
38. Docquier, D. et al. A comparison of two causal methods in the context of climate analyses. *Nonlinear Process Geophys.* **31**, 115–136 (2024).
39. Su, J., Chen, D., Zheng, D., Su, Y. & Li, X. The insight of why: causal inference in earth system science. *Sci. China Earth Sci.* **66**, 2169–2186 (2023).
40. Granger, C. W. Investigating causal relations by econometric models and cross-spectral methods. *Econometrica* **37**, 424–438 (1969).
41. Bach, E., Motesharrei, S., Kalnay, E. & Ruiz-Barradas, A. Local atmosphere–ocean predictability: dynamical origins, lead times, and seasonality. *J. Clim.* **32**, 7507–7519 (2019).
42. Yang, X., Wang, Z.-H., Wang, C. & Lai, Y.-C. Finding causal gateways of precipitation over the contiguous United States. *Geophys. Res. Lett.* **50**, e2022GL101942 (2023).
43. Sugihara, G. et al. Detecting causality in complex ecosystems. *Science* **338**, 496–500 (2012).
44. Vannitsem, S. & Ekelmans, P. Causal dependences between the coupled ocean–atmosphere dynamics over the tropical Pacific, the North Pacific, and the north Atlantic. *Earth Syst. Dyn.* **9**, 1063–1083 (2018).
45. Wang, Y., Yang, X. & Wang, Z.-H. Causal mediation of urban temperature by geopotential height in us cities. *Sustain. Cities Soc.* **100**, 105010 (2024).
46. Runge, J. Causal network reconstruction from time series: from theoretical assumptions to practical estimation. *Chaos* **28,**075310 (2018).
47. Di Capua, G. et al. Dominant patterns of interaction between the tropics and mid-latitudes in boreal summer: Causal relationships and the role of time-scales. *Weather Clim. Dyn. Discuss.* **2020**, 1–28 (2020).

48. Pfleiderer, P., Schleussner, C.-F., Geiger, T. & Kretschmer, M. Robust predictors for seasonal Atlantic hurricane activity identified with causal effect networks. *Weather Clim. Dyn.* **1**, 313–324 (2020).
49. Kretschmer, M., Runge, J. & Coumou, D. Early prediction of extreme stratospheric polar vortex states based on causal precursors. *Geophys. Res. Lett.* **44**, 8592–8600 (2017).
50. Hatzaki, M. et al. Causal drivers of Mediterranean winter climate variability. *Environ. Sci. Proc.* **26**, 155 (2023).
51. Sharma, D., Das, S. & Goswami, B. Variability and predictability of the Northeast India summer monsoon rainfall. *Int. J. Climatol.* **43**, 5248–5268 (2023).
52. Hersbach, H. et al. ERA5 hourly data on single levels from 1940 to present. *Copernicus Climate Change Service (C3S) Climate Data Store (CDS)* (2023).
53. Tian, Y. et al. Radiation as the dominant cause of high-temperature extremes on the eastern Tibetan Plateau. *Environ. Res. Lett.* **18**, 074007 (2023).
54. Seneviratne, S. I. et al. Investigating soil moisture–climate interactions in a changing climate: a review. *Earth Sci. Rev.* **99**, 125–161 (2010).
55. Bárdossy, A. & Caspary, H. Detection of climate change in Europe by analyzing European atmospheric circulation patterns from 1881 to 1989. *Theor. Appl. Climatol.* **42**, 155–167 (1990).
56. Drobinski, P. et al. Scaling precipitation extremes with temperature in the Mediterranean: past climate assessment and projection in anthropogenic scenarios. *Clim. Dyn.* **51**, 1237–1257 (2018).
57. Orth, R. & Seneviratne, S. I. Analysis of soil moisture memory from observations in Europe. *J. Geophys. Res.* **117**, D15115 (2012).
58. Duchez, A. et al. Drivers of exceptionally cold North Atlantic Ocean temperatures and their link to the 2015 European heat wave. *Environ. Res. Lett.* **11**, 074004 (2016).
59. Trenberth, K. E. & Shea, D. J. Relationships between precipitation and surface temperature. *Geophys. Res. Lett.* **32**, L14703 (2005).
60. Seneviratne, S. I., Lüthi, D., Litschi, M. & Schär, C. Land–atmosphere coupling and climate change in Europe. *Nature* **443**, 205–209 (2006).
61. Berg, A. et al. Interannual coupling between summertime surface temperature and precipitation over land: Processes and implications for climate change. *J. Clim.* **28**, 1308–1328 (2015).
62. Vautard, R. et al. Heat extremes in Western Europe are increasing faster than simulated due to missed atmospheric circulation trends. *Nat. Commun.* **14**, 6803 (2023).
63. Suarez-Gutierrez, L., Müller, W. A., Li, C. & Marotzke, J. Dynamical and thermodynamical drivers of variability in European summer heat extremes. *Clim. Dyn.* **54**, 4351–4366 (2020).
64. Emori, S. & Brown, S. Dynamic and thermodynamic changes in mean and extreme precipitation under changed climate. *Geophys. Res. Lett.* **32**, L17706 (2005).
65. Shah, J. et al. Increasing footprint of climate warming on flash droughts occurrence in Europe. *Environ. Res. Lett.* **17**, 064017 (2022).
66. Bartusek, S., Kornhuber, K. & Ting, M. 2021 North American heatwave amplified by climate change-driven nonlinear interactions. *Nat. Clim. Change* **12**, 1143–1150 (2022).
67. Zhou, S. et al. Land–atmosphere feedbacks exacerbate concurrent soil drought and atmospheric aridity. *Proc. Natl. Acad. Sci.* **116**, 18848–18853 (2019).
68. Zscheischler, J., Orth, R. & Seneviratne, S. I. A submonthly database for detecting changes in vegetation-atmosphere coupling. *Geophys. Res. Lett.* **42**, 9816–9824 (2015).
69. Dai, A. Increasing drought under global warming in observations and models. *Nat. Clim. Change* **3**, 52–58 (2013).
70. Vautard, R. et al. The European climate under a 2 °C global warming. *Environ. Res. Lett.* **9**, 034006 (2014).
71. Li, J. et al. A standardized index for assessing sub-monthly compound dry and hot conditions with application in China. *Hydrol. Earth Syst. Sci.* **25**, 1587–1601 (2021).
72. Bateni, M. M. M., Behmanesh, J., De Michele, C., Bazrafshan, J. & Rezaie, H. Composite agrometeorological drought index accounting for seasonality and autocorrelation. *J. Hydrol. Eng.* **23**, https://doi.org/10.1061/%28ASCE%29HE.1943-5584.0001654 (2017).
73. Salvadori, G., De Michele, C., Kottegoda, N. T. & Rosso, R. *Extremes in Nature: an Approach Using Copulas*, vol. 56 (Springer Science & Business Media, 2007).
74. Runge, J., Petoukhov, V. & Kurths, J. Quantifying the strength and delay of climatic interactions: the ambiguities of cross correlation and a novel measure based on graphical models. *J. Clim.* **27**, 720–739 (2014).
75. Runge, J., Nowack, P., Kretschmer, M., Flaxman, S. & Sejdinovic, D. Detecting and quantifying causal associations in large nonlinear time series datasets. *Sci. Adv.* **5**, eaau4996 (2019).
76. Benjamini, Y. & Hochberg, Y. Controlling the false discovery rate: a practical and powerful approach to multiple testing. *J. R. Stat. Soc. Ser. B (Methodol.)* **57**, 289–300 (1995).
77. Benjamini, Y. & Yekutieli, D. The control of the false discovery rate in multiple testing under dependency. *Ann. Stat.* **29**, 1165–1188 (2001).
78. Runge, J. et al. Identifying causal gateways and mediators in complex spatio-temporal systems. *Nat. Commun.* **6**, 8502 (2015).
79. Wilks, D. S. *Statistical Methods in the Atmospheric Sciences*, vol. 100 (Academic Press, 2011).
80. Di Capua, G. et al. Long-lead statistical forecasts of the Indian summer monsoon rainfall based on causal precursors. *Weather Forecast.* **34**, 1377–1394 (2019).
81. Di Capua, G. & Coumou, D. Changes in meandering of the Northern Hemisphere circulation. *Environ. Res. Lett.* **11**, 094028 (2016).

Acknowledgements

This work emerged from the 2nd Como Training School on Statistical Modelling of Compound Events (26 September–7 October 2022), supported by T.I.M.E (Top International Managers in Engineering), European COST Action DAMOCLES (CA17109), and Regione Lombardia. This research has been supported by the German Federal Ministry for Education and Research (BMBF) via ClimXtreme project (subproject PERSEVERE, phase 2nd, grant no. 01LP2322D) (Y.T.), the JPI Climate/JPI Oceans project ROADMAP (grant no. 01LP2002B) (G.D.C.), and the ClimXtreme project (subproject PERSEVERE, grant no. 01LP1901E) (G.D.C.). This research has been supported by the RETURN project (Multi-risk science for resilient communities under a changing climate) with Extended Partnership, which received funding from the European Union Next-GenerationEU, National Recovery and Resilience Plan-NRRP, Mission 4, Component 2, Investment 1.3-D.D. 1243 2/8/2022, PE0000005 (C.D.M.). This research has been supported by the European Union's Horizon 2020 research and innovation programme (Grant Agreement No. 101003276) (J.N.C.).

Author contributions

Y.T. and D.G. led the conceptualization, methodology development, investigation, visualization, and writing of the original draft, as well as contributed to the review and editing. G.D.C. and C.D.M. played a central role in the conceptualization, methodology development, analysis, supervision, review, and editing. J.N.C. contributed to draft writing, visualization, review, and editing. J.A. and H.L. contributed to writing, review, and editing process.

Funding

Open Access funding enabled and organized by Projekt DEAL.

Competing interests

The authors declare no competing interests.

Additional information

Supplementary information The online version contains supplementary material available at https://doi.org/10.1038/s43247-024-01934-2.

Correspondence and requests for materials should be addressed to Yinglin Tian.

Peer review information *Communications Earth & Environment* thanks the anonymous reviewers for their contribution to the peer review of this work. Primary Handling Editors: Akintomide Akinsanola and Alireza Bahadori. A peer review file is available

Reprints and permissions information is available at http://www.nature.com/reprints

Publisher's note Springer Nature remains neutral with regard to jurisdictional claims in published maps and institutional affiliations.

Open Access This article is licensed under a Creative Commons Attribution 4.0 International License, which permits use, sharing, adaptation, distribution and reproduction in any medium or format, as long as you give appropriate credit to the original author(s) and the source, provide a link to the Creative Commons licence, and indicate if changes were made. The images or other third party material in this article are included in the article's Creative Commons licence, unless indicated otherwise in a credit line to the material. If material is not included in the article's Creative Commons licence and your intended use is not permitted by statutory regulation or exceeds the permitted use, you will need to obtain permission directly from the copyright holder. To view a copy of this licence, visit http://creativecommons.org/licenses/by/4.0/.

© The Author(s) 2024